Review Article

Stephen Ho*, Kitty Kumar, Kenneth K.C. Lee, Jianzhao Li and Peter R. Herman

Interferometric femtosecond laser processing for nanostructuring inside thin film

Abstract: Femtosecond laser interactions inside transparent dielectric films of refractive index, n_{film}, with tight focusing presents strong nonlinear interactions that can be preferentially confined at the fringe maxima as formed by Fabry-Perot interference, to generate thin nanoscale plasma disks separated on half-wavelength, $\lambda/2n_{film}$. The nano-thin disk explosions can be controlled inside the film to cleave open subwavelength internal cavities at single or multiple periodic depths at low laser exposure, while higher exposure will eject a quantised number of film segments with segment thickness defined by the laser wavelength. This new method enables high-resolution film patterning for ejecting nanodisks at quantised film depth for colouring and three-dimensional (3D) surface structuring, as well as for fabrication of free-standing nanofilms.

Keywords: laser materials processing; optical properties; plasmas; thin films; thin film devices and applications; ultrafast lasers.

DOI 10.1515/aot-2014-0047
Received September 15, 2014; accepted October 27, 2014

1 Introduction

High-resolution writing inside thin films is a new and challenging field of research. In this direction, various laser interference methods have been developed to write subwavelength features inside photosensitive materials ranging from holography for the fabrication of photonic crystals [1] to two-beam interference for fibre Bragg gratings [2]. These processing methods harness optical patterns as generated with various forms of interferometry, including phase masks, diffraction gratings, prisms or partial reflecting mirrors to split and recombine light and create multiple beams.

Transparent thin films are well known to generate standing wave patterns that build over multiple Fresnel reflections at the interfaces, for example, as seen in soap bubbles, insects, microelectronic circuits, optical storage disks, and multilayered dielectric stacks. Such interference has been observed to modify the laser breakdown threshold for damage in single layer dielectric [3, 4] and multilayered dielectric films [5] by enhancing the internal laser light intensity. Similar interference effects were also inferred by Hosokawa and co-authors [6, 7] to underlie a periodic ablation rate in Cu-phthalocyanine amorphous thin films. However, laser ablative structuring internally in such transparent films has not been reported on such interference patterns until recently. In reference [8], we reported the first demonstration of quantised structuring of dielectric films, harnessing thin film interference effects to concentrate femtosecond pulsed laser light into the highly contrasting fringes. In this way, thin nanodisks of plasma were generated by the strong nonlinear laser interactions on the ultrashort time scale of the femtosecond laser duration. The plasma nanodisks were connected with the cleaving and fragmentation observed in the thin film. The plasma disks thus are a new approach to open nanocavities, and enable quantised etching from laser-material modification zones much smaller than the laser wavelength, and without deleterious thermal diffusion effects.

In this paper, we briefly review laser direct writing inside thin films and the concepts underlying the new method of interferometric laser structuring. The control over the ejection of quantised segments to digitally excise fractional film depths, or to create nanoblisters that open nanocavities inside the film, is presented for SiN_x

***Corresponding author: Stephen Ho,** Edward S. Rogers Sr. Department of Electrical and Computer Engineering, University of Toronto, 10 King's College Road, Toronto, Ontario M5S 3G4, Canada, e-mail: stephen.ho@utoronto.ca
Kenneth K.C. Lee, Jianzhao Li and Peter R. Herman: Edward S. Rogers Sr. Department of Electrical and Computer Engineering, University of Toronto, 10 King's College Road, Toronto, Ontario M5S 3G4, Canada
Kitty Kumar: Wyss Institute for Biologically Inspired Engineering, Harvard University, Boston, MA, USA

films. We extend beyond our prior study [8] to examine the wavelength dependence of the quantised internal structuring and further harness a higher pulse energy to enable larger area processing over a broader range of film thicknesses. A better understanding of the laser-material interaction underlying this new processing technique is examined towards the prospects for the fabrication of nanofluids, microlenses, freestanding thin films and lab-in-film devices. The quantised structuring of a thin film on a substrate can also be employed for marking and colouring devices.

2 Background

A major industry trend is currently exploiting ultrashort-pulsed lasers, particularly with pulse duration in the picosecond and femtosecond domain, that is directed towards new applications in processing of bulk and thin films of transparent dielectrics, as found on microelectronic wafers, optical display, light emitters and photovoltaic cells. Inside a thick transparent dielectric medium, ultrashort laser light can be confined in a volume smaller than the diffraction-limited radius and Rayleigh length of the focal volume as created by a high numerical aperture (NA) lens. For example, in the case of a Gaussian shaped laser beam of wavelength, λ, the focal volume can be narrowed to a beam waist of radius $\omega_o=\lambda/\pi NA$ ($1/e^2$ irradiance) over a short depth of focus of $d_f=2\lambda/\pi NA^2$ (Rayleigh range) to drive strong and highly localised nonlinear absorption. This tight confinement of light has been applied to locally excite multiphoton fluorescence in living cells and enable high-resolution three-dimensional (3D) microscopy [9]. In dielectric materials, this focusing can induce gentle refractive index changes for writing of 3D optical circuits [10] or drive microexplosions for 3D memory storage or marking [11, 12].

In the case of thin transparent films, subwavelength size features can be recorded, by inducing gentle material modification in the material, that are localised at the peak intensity positions of the highly contrasting optical fringe pattern generated by the interference of laser light with itself. This technique has been used to record holographic or volume grating patterns in photographic film, to fabricate Bragg gratings in the core waveguide of optical silica fibre [2] and to shape 3D photonic crystal templates inside a photoresist [1]. The high-resolution recording may be further assisted by a short temporal pulse during which there is minimal thermal dissipation to diffuse and expand the laser interaction zone.

Alternatively, focused ultrashort laser light has been used to selectively eject thin dielectric films from an underlying substrate driven by strong light-material interaction at the buried substrate-dielectric interface [13–18]. In this case, the short penetration depth of laser light in the underlying substrate confines the light-material interaction to a very narrow zone in comparison with the long depth of focus. Depending on the laser energy dissipated in the thin interaction zone, the complete thickness of the dielectric film can be released to delaminate from the substrate and form a thin-film blister at low laser exposure, or the full film thickness can be ejected from the interface at higher exposure. This type of complete, yet selective ejection of dielectric film from the substrate has promised a wide range of new applications that include patterning and repair in microelectronic circuits, photovoltaic cells [19] and glass display manufacturing. The ejection phenomenon further underlies the driving mechanisms in laser induced forward transfer [20] for printing or additive manufacturing, and cell ejection by laser pressure catapulting [9, 21].

Extension of such ablative processing from an interface to the inside volume of the transparent film has remained highly challenging and otherwise been dominated by the gentle photosensitive processes discussed above. A localised laser interaction can be expected when interference fringes form in a thin film of refractive index, n_{film}, and thickness, d, to provide high intensity (maxima) interaction zones separated by the fringe spacing of $\lambda/2n_{film}$. However, even when Fresnel reflections are sufficiently strong to generate highly contrasting interference fringes, these isolated interaction zones are expected to wash away due to thermal diffusion if the laser-material interaction time is of the order of thermal diffusion length scale. In the femtosecond regime, these interaction zones were observed to remain isolated during the laser interaction time and manifest in cleanly cleaved $\lambda/2n_{film}$-thick segments inside the film. The method promised new means to create buried and open microchannels, reservoirs, large membrane structures, optical elements such as blazed gratings and Fresnel lenses [8]. We also demonstrated how the quantised fractional removal of film segments at digital depths was able to generate a variety of vibrant colours that are broadly attractive for marking and labelling. In this paper, we examine a broader range of film colouring effects accounting for both film thinning and Fresnel phase-shifts on nanocavity formation. Quantised structuring is extended to various laser wavelengths for a variety of film thicknesses and for exposures at comparatively higher pulse energy than previously reported. We also have extended the computational study of the underling laser-material interaction to identify the role of

critical density in quantised structuring of thin dielectric films at different laser wavelengths. We predict the formation of narrow (<20 nm thick) plasma zones within the film that reach a threshold for film cleavage commensurate with the calculated plasma density reaching critical.

3 Materials and methods

Thin films of SiN_x films were grown to 500 nm–800 nm thicknesses by plasma-enhanced chemical vapour deposition (Oxford Instruments, PlasmaLab 100) over substrates of polished phosphorus-doped (001) crystalline silicon wafers of 400-μm thickness. In this arrangement, optical interference can only build up in the SiN_x layer for the sub-picosecond laser pulses applied in this study. Detailed fabrication conditions can be found in Kumar et al. [8].

Three different laser systems were applied to study quantised structuring of the SiN_x films over a range of wavelengths, pulse durations and pulse energies, as presented in Table 1. Only single pulse exposures were studied at each exposure site to avoid the strong effects of changing film thickness and morphology by prior laser pulses. A fibre-amplified laser (IMRA America, μJewel D-400-VR) provided single Gaussian-shaped laser pulses (M^2=1.33) at 1045 nm and 522 nm wavelengths. Single pulses were selected with an external acousto-optic modulator and applied to the SiNx interface at variable pulse energy, in ranges of 10 nJ–1150 nJ at 1045 nm and 5 nJ–700 nJ at 522 nm. An aspherical lens of focal length f=15.4 mm (at 1045 nm) and a plano-convex lens of focal length f=8 mm (at 522 nm) provided radial spot sizes ($1/e^2$) of ω_o=3.4 μm and ω_o=0.495 μm, respectively, which could also be expanded to diameters as large as 45.6 μm and 154.8 μm, respectively, by moving the target above or below the focal plane. Fluence exposures were controlled by focal position and variable pulse energy to ranges of 0.61 mJ/cm²–3.16 J/cm² at 1045 nm and 26.5 μJ/cm²–90.9 J/cm² at 522 nm. Alternatively, the frequency doubled 522-nm laser beam of ~4.5-mm diameter was masked with a circular aperture of 1-mm diameter positioned at ~115 cm distance before an aspherical lens of focal length f=2.8 mm, and thereby provided a partially uniform imaging profile of a 2.4-μm diameter top-hat beam.

A second fibre laser system (Amplitude Systemes, Satsuma) provided Gaussian-shaped pulses (M^2=1.14) of 515 nm wavelength at energies variable from 10 nJ to 1670 nJ. An aspherical lens of focal length f=11 mm provided a spot size of ω_o=0.8 μm. By varying the pulse energy and the target surface position at the focus (±200 μm axial shift), fluences of 0.17 mJ/cm²–79.9 J/cm² were delivered to the SiN_x surface.

Lastly, a Ti:Sapphire laser provided 800 nm femtosecond light at significantly higher pulse energies, from 0.705 μJ to 12.30 μJ, in a Gaussian-shaped beam (M^2≈1.3). An objective lens of focal length f=50 mm formed a focal radial spot size ($1/e^2$) of ω_o=4.7 μm, which was shifted from 1 mm below to 1 mm above the sample surface to provide fluence exposures in the range of 5.8 mJ/cm²–17.7 J/cm² on the SiN_x surface. Samples were mounted and precisely calibrated to align with the focal plane of the respective lenses using a precise beam delivery, imaging and motion stage (Aerotech ABL1000) system. Single laser pulses were applied to isolate interaction spots.

The surface morphologies of the laser-irradiated samples were inspected by optical microscopy, atomic force microscopy and scanning electron microscopy (SEM). A thin layer (~4 nm) of gold coating was deposited prior to SEM imaging to reduce charging effects. Select samples were further cut axially by a focused ion beam (Zeiss NVision 40) to provide cross-sectional SEM images.

An intensified charge-coupled device camera (ICCD) (Andor, iStar DH734-18U-03), synchronised to the 522-nm laser pulse with a delay generator (Stanford Research Systems DG535), was used to capture time-resolved 2D side-view images of the laser ablation plume through a 50× microscope objective lens. Plume emissions from a 500-nm thick SiN_x film were followed over a wide range of laser exposures (50 nJ–380 nJ) with gate widths varied from 3 ns to 50 ns and time delays from 0 μs to 2 μs.

Table 1 Laser specifications applied in quantised structuring of SiN_x film.

Laser	Repetition rate (kHz)	Wavelength (nm)	Pulse duration (fs)	M^2	Applied pulse energies (μJ)
IMRA FCPA (μJewel D-400-VR)	100	1045	340	1.33	0.010–1.150
		522	200		0.005–0.700
Amplitude Systemes (Satsuma)	100	515	215	1.14	0.010–1.670
Ti:Sapphire laser (Spectra-Physics Spitfire Pro 40F)	0.01	800	50	1.3	0.705–12.30

4 Quantised film structuring

We first examine the laser-plasma generation in SiN_x dielectric films as formed by ultrafast laser nonlinear interactions when modulated periodically by thin film interference effects. The morphology of laser-irradiated films is studied over a range of wavelengths and compared with a laser-plasma model to verify the principle of nanoplasma disk generation at the expected interference fringe maxima.

4.1 Plasma modeling on Fabry-Perot interference

Strong Fabry-Perot interference can be established by focusing laser light into a thin transparent film with a thickness $>\lambda/4n_{film}$ when there is sufficient Fresnel reflection at the air/film and the film/substrate interfaces. Inside the SiN_x film ($n_{film}\approx2.0$ for λ=515 nm and 1045 nm) of d=800 nm thickness on a silicon substrate ($n_{Si}\approx4.2$ and $\kappa_{Si}\approx0.04$ for λ=515 nm and $n_{Si}\approx3.6$ and $\kappa_{Si}\sim0.001$ for λ=1045 nm), one anticipates laser wavelengths of λ=515 nm and 1045 nm to generate six and three fringe maxima $m=\lfloor d/(\lambda/2n_{film})\rfloor$, respectively, with fringe spacings of $\lambda/2n_{film}$=128.8 nm and 261.3 nm at λ=515 nm and 1045 nm, respectively. Optical interference calculations are presented across the film in Figure 1A–C that correspond to respective exposures of 515 nm, 1045 nm and 1045 nm wavelength at incident intensities of I_o=4.38×10^{12} W/cm^2, 4.24×10^{12} W/cm^2 and 1.15×10^{13} W/cm^2, respectively. The intensities for Figure 1A and B correspond closely with the threshold laser modification for the 800 nm film, as discussed further below. These incident intensities yield internal peak intensities of I_{int}=3.18×10^{12} W/cm^2, 2.82×10^{12} W/cm^2 and 7.24×10^{12} W/cm^2, respectively, while relatively strong Fresnel reflections yield contrasting interference fringes with visibilities of 0.64, 0.54 and 0.54 in Figure 1A–C, respectively. In all cases, a node is positioned near the SiN_x/Si interface due to the out-of-phase Fresnel reflection which locks the last fringe maximum at a position of $\lambda/4n_{film}\approx$64.4 nm (for λ=515 nm) and 130.6 nm (for λ=1045 nm) from this bottom interface. As a consequence, the position for the first fringe maximum will vary with the film thickness to the calculated positions of d-(m-0.5)$\lambda/2n_{film}$=91.9 nm for λ=515 nm and 146.9 nm for λ=1045 nm from the air/SiN_x interface as shown in Figure 1A–C, respectively.

The intensity profiles as shown in Figure 1A–C can be further applied to predict the electron density profile generated by nonlinear optical interactions inside the film for localising internal structuring. The beam energy becomes divided into thin interaction zones that align with the fringe intensity maxima, resulting in quantised internal structuring of the thin film or ejection of film segments as verified in the SEM morphology of Figure 1D–F. Here, we extend the modelling in Kumar et al. [8] to multiple wavelengths and thicker film thickness.

For short duration laser pulses, nonlinear light interactions inside the transparent dielectric film will be dominated by multiphoton absorption and electron avalanche that ionises atoms to create an electron density, n_e, according to Eq. (1) [22]:

$$\frac{dn_e(t)}{dt}=n_e(t)w_{imp}+N_a w_{mpi}-\frac{n_e(t)}{\tau_r} \tag{1}$$

where N_a is the neutral atomic density and τ_r is the electron relaxation time. This multiphoton ionisation (MPI) and electron avalanche are typically found to dominate in transparent dielectrics as the main absorption mechanisms with ultrashort laser pulses of around 100 fs duration when applied at our 10^{12} W/cm^2–10^{13} W/cm^2 intensity range [22]. The impact ionisation rate (w_{imp}) and MPI rate (w_{mpi}), at the incident laser intensity, I_o, are given by Eqs. (2) and (3), respectively [22]:

$$w_{imp}\approx\frac{\varepsilon_{osc}}{J_i}\frac{2\omega^2\nu_{eff}}{\nu_{eff}^2+\omega^2} \tag{2}$$

$$w_{mpi}\approx\omega N^{\frac{3}{2}}\left(\frac{\varepsilon_{osc}}{2J_i}\right)^N \tag{3}$$

where the electron quiver energy, ε_{osc}, and effective electron collision time, $\tau_{eff}=1/\nu_{eff}$, (ν_{eff} is the collision frequency) are calculated by Eqs. (4) [23] and (5) [22], respectively:

$$\varepsilon_{osc}[eV]=\frac{e^2\varepsilon^2}{4m_e\omega^2}=9.34\frac{I}{10^{14}[Wcm^{-2}]}\lambda^2[\mu m] \tag{4}$$

$$\tau_{eff}=\frac{1}{\nu_{eff}}=\frac{16\varepsilon_o^2\sqrt{m_e^*(0.1E_g)^3}}{\sqrt{2}e^4n_e(t)} \tag{5}$$

For SiN_x, the electron density was computed for values of N_a=8×10^{22} cm^{-3} for the atomic density, E_g=5.3 eV for the bandgap [24], J_i=E_g=5.3 eV for the ionisation potential, and $m_e^*=m_e$ for the effective electron mass. For each laser frequency, $\omega=2\pi c/\lambda$, the order of nonlinear MPI in the simulations of Figure 1A–C was calculated from $N=\lceil J_i/\hbar\omega\rceil$ to yield N=3 for λ=515 nm (Figure 1A) and N=5 for 1045 nm (Figure 1B and C).

Electron densities were calculated from Eq. (1) for incident laser intensities found sufficient to just reach or exceed the plasma critical densities of n_{cr}=4.1×10^{21} cm^{-3} for λ=515 nm

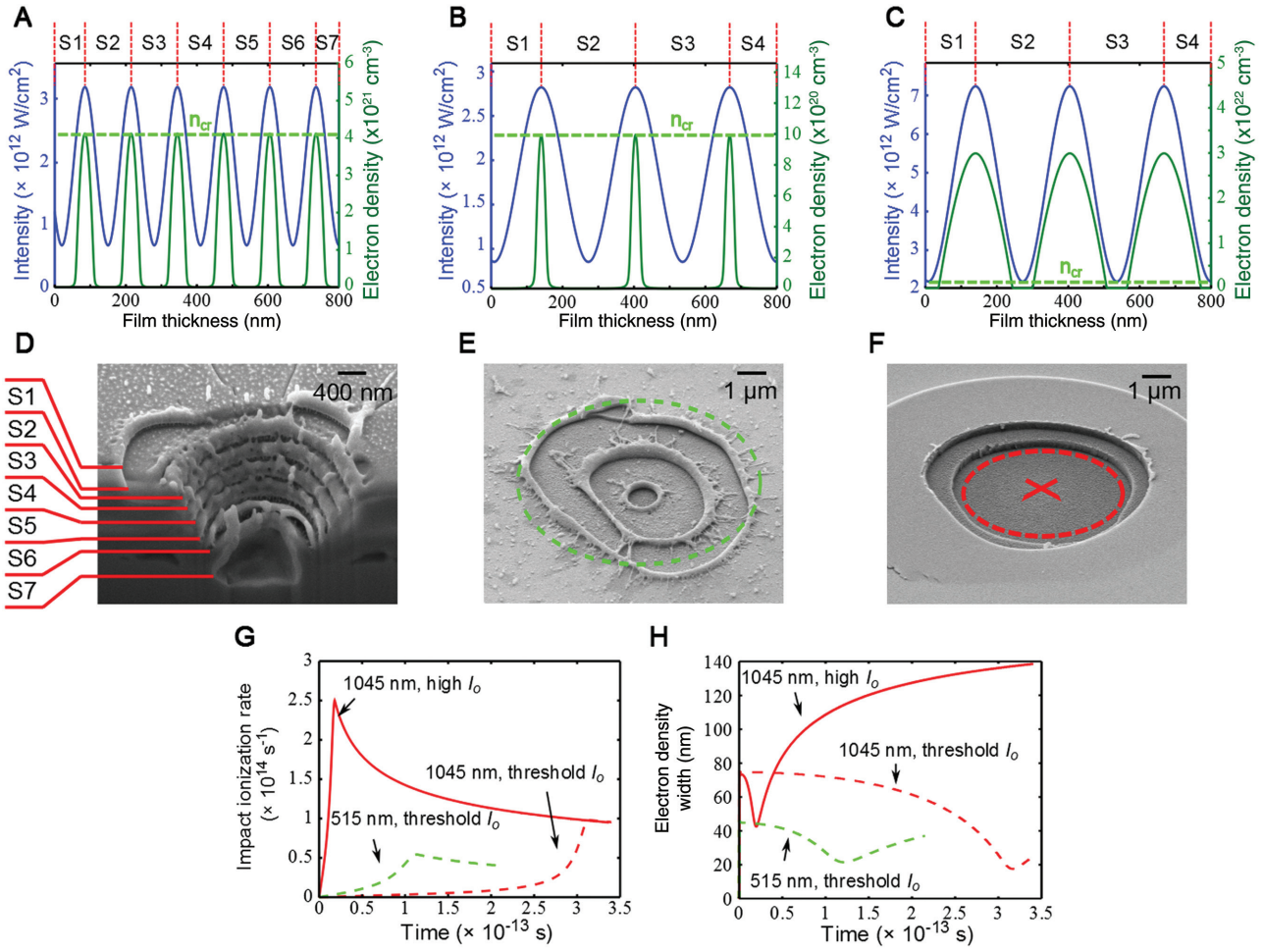

Figure 1 The simulation results illustrating the modulated intensity profiles (blue lines) together with the electron density profile (green lines) calculated for a Gaussian-shaped pulse incident on 800 nm thick SiN_x film as a result of the interference of Fresnel reflections from the boundary interfaces for wavelengths of (A) 515 nm and (B, C) 1045 nm, where (A) and (B) were simulated at threshold incident intensities I_o=of 4.38×10^{12} W/cm^2 and 4.24×10^{12} W/cm^2, respectively, for the electron density to just reach the critical plasma density (n_{cr}) and where (C) was simulated at high incident intensity of I_o=1.15×10^{13} W/cm^2 to exceed n_{cr} at the fringe maxima positions. The scanning electron microscopy (SEM) images show 800 nm thick SiN_x films exposed by fluences of 76.7 J/cm^2, 4.4 J/cm^2 and 2.0 J/cm^2 at 515 nm, 515 nm and 1045 nm wavelengths, respectively, in (D) cross-sectional, (E) oblique top and (F) oblique top views, respectively. The green dashed line in (E) identifies a 3.67 μm radial beam position for delivery of the threshold intensity. The red cross and the dashed line in (F) correspond, respectively, to a peak exposure intensity of 1.15×10^{13} W/cm^2 at the beam centre and the radial beam position of 2.95 μm for threshold intensity exposure. The time evolution of the impact ionisation rates (G) for 515 nm at threshold I_o (green dashed line), 1045 nm at threshold I_o (red dashed line) and 1045 nm at 2.7× threshold I_o (red line), which compare with constant multiphoton ionisation (MPI) rates of w_{mpi}=7.71×10^9 s^{-1} at threshold I_o for 515 nm, w_{mpi}=2.91×10^8 s^{-1} at threshold I_o for 1045 nm and w_{mpi}=2.23×10^{10} s^{-1} at high I_o for 1045 nm. The time evolution for the thicknesses (H) of the laser-plasma zones (full width half maximum of the electron density profile) are plotted for 215 fs pulse duration 515-nm light and 340 fs duration 1045-nm light, showing minimum widths of 21.4 nm (green dashed line), 17.5 nm (red dashed line) and 42.8 nm (red line) at times of 122 fs, 213 fs and 18 fs, respectively. The widths were calculated for threshold I_o, threshold I_o and 2.7×threshold I_o, respectively, that correspond with the time at which the impact ionisation rates have peaked at the fringe maxima, and being diminishing. S1 to S7 represents film separated into seven $\lambda/2n_{film}$ segments.

and 1.0×10^{21} cm^{-3} for λ=1045 nm and are presented (dashed lines) in Figure 1A and B, respectively. This approach yielded internal peak intensities of I_{int}=3.18×10^{12} W/cm^2 at 515 nm and 2.82×10^{12} W/cm^2 at 1045 nm. In the threshold internal intensity calculations, the electron relaxation in Eq. (1) was ignored, since the majority of electrons were generated by impact ionisation during the last 34 fs and 99 fs duration, respectively, of the 215-fs and 340-fs laser pulse durations, respectively. Here, we do not anticipate the electron relaxation time of SiN_x to be shorter than the fast τ_r=170 fs value as reported [25] for wider bandgap fused silica. A longer 290-fs period of dominant impact

ionisation was found in the case of 1045 nm exposure in Figure 1C, where only a small 2.7× higher exposure of I_{int}=7.24×10^{12} W/cm^2 generated a significantly higher (~30×) electron density of 2.99×10^{22} cm^{-3}. Electron recombination may be expected to lower this value slightly.

The impact ionisation rates were calculated with Eq. (2) and plotted in Figure 1G as a function of time for each of the cases of electron density calculated in Figure 1A–C. The rates grow strongly with growing electron density, before peaking and falling slowly as the electron collision frequency [Eq. (5)] exceeds the laser frequency. This fall off of impact ionisation in the later stages of laser interaction prevents an otherwise unrealistic exponential growth of the electron density. For all cases of exposure, the average impact ionisation rates in the range of 0.3×10^{14} s^{-1}–1.2×10^{14} s^{-1} in Figure 1G are found to dominate in the laser interaction process, dramatically exceeding the calculated [Eq. (3)] MPI rates of w_{mpi}=7.71×10^9 s^{-1} (threshold I_{int} at 515 nm), 2.91×10^8 s^{-1} (threshold I_{int} at 1045 nm) and 2.23×10^{10} s^{-1} (2.7× threshold I_{int} at 1045 nm).

The morphologies of laser-irradiated SiN_x films are presented in Figure 1D–F for Gaussian beam exposures at 515 nm, 515 nm and 1045 nm wavelength, respectively, of spot radii (1/e^2) of 0.83 μm, 3.48 μm and 4.30 μm, respectively, with respective pulse energies of 1.67 μJ, 1.67 μJ and 1.15 μJ. The calculated incident peak intensities of I_o=7.16×10^{14} W/cm^2, 4.07×10^{13} W/cm^2 and 1.15×10^{13} W/cm^2, respectively, exceed the threshold values of I_o=4.38×10^{12} W/cm^2 (Figure 1A) for the 515 nm case and 4.24×10^{12} W/cm^2 (Figure 1B) for the 1045 nm cases. As predicted by the simulation, the annular structures in the SEM cross-sectional image in Figure 1D provides definitive evidence of laser-generated plasma disks as forming on periodic cleavage planes inside the film at the expected fringe maxima positions shown in Figure 1A. A total of seven layer segments are clearly delineated with thicknesses commensurate with the expected $\lambda/2n_{film}$=128.8 nm fringe spacing. A strong interaction is further found to have occurred at the SiN_x/Si interface, from which segment 7 has been cleanly ejected in the 1.1-μm diameter central zone of the laser-irradiated spot.

By reducing the peak incident intensity exposure ~18-fold with a weaker focusing condition, Figure 1E reveals the removal of the first, second and third segments with 515-nm wavelength light, forming concentric rings of decreasing diameter that line up with a rising intensity over the Gaussian beam profile of radius ω_o=3.48 μm. The ejection of the first segment is terminated with the formation of an outer melt lip at a radius of 3.50 μm in Figure 1E, which corresponds closely with the laser pulse radius (1/e^2). Applying threshold incident intensity of I_o=4.38×10^{12} W/cm^2, as found in Figure 1A to surpass the critical density, into a Gaussian beam analysis for the present Figure 1E, one finds a radius of 3.67 μm to demark this threshold for driving critical density. This radius is marked by the green dashed line in Figure 1E, and found to align closely with the observed first segment melt radius of 3.50 μm. This close correspondence supports the role of critical plasma density in defining the threshold for material damage as also previously recognised in ultrafast laser interactions in dielectrics [5, 22, 23]. Hence, the simple MPI and avalanche model [Eq. (1)–Eq. (5)] is seen to provide a useful estimate of the threshold laser exposure, connecting the critical plasma density with the threshold for interference-driven film cleavage.

The present laser interactions are repetitively formed in periodic disks, internally in the film, that underlie the observations of quantised laser film ejection at the fringe maxima positions. It is instructive to follow the time evolution of the electron density 'fringes' for the exposure conditions in Figure 1A–C. The width of these anticipated electron plasma disks (full width half maximum) were calculated and plotted in Figure 1H as a function of time. For the case of threshold exposure at 515 nm, the electron plasma forms initially with a 45.0-nm width, narrowed by the multiphoton processes on the optical fringe maxima. The width narrows further to 21.4 nm at 122 fs, corresponding to the time at which the impact ionisation rate reaches a maximum, as seen in Figure 1G for the threshold exposure at 515 nm wavelength (green dashed line). Thereafter, the electron density width broadens in Figure 1H, reaching 37.0 nm at the end of the 215-fs pulse as avalanche ionisation catches up on the lower intensity sides of the fringe maxima. Throughout the interaction, the plasma width remains significantly smaller than the 128.8 nm value of optical fringe period, therefore underpinning the concept of microexplosion driven from a new planar disk type of geometry.

Further evaluation of the hydrodynamics of the SiN_x film following the formation of thin-plasma disks would involve significantly more elaborate computations beyond the scope of the present paper. However, one can consider a simple view of thermal dynamics that would follow from the rapid formation of the thin explosive plasma disks. For 515-nm wavelength irradiation at threshold, a critical plasma density of n_{cr}=4.1×10^{21} cm^{-3} was found to form with a 37.0 nm thickness for the case in Figure 1A. Following a rapid electron-ion relaxation, this electron density presents a peak temperature estimate of ~2450°C if we equate the temperature rise, ΔT, with the dissipated laser energy density, ρ_E, according to $\Delta T=\rho_E/C_{SiN_x}$, where C_{SiN_x}=1.96 J/cm^3°C can be used for the volumetric heat

capacity. A conservative estimate of the energy density can be found according to the number of electrons generated by 3-photon ionisation from $\rho_E=3E_{ph}n_{cr}$, where the photon energy is E_{ph}=2.4 eV for 515 nm light. The time for thermal diffusion to propagate one-half of the fringe spacing ($\lambda/4n_{film}$) and thus washout the periodic 'heat' disks is found from $\tau_d=\lambda^2/64n_{film}^2D$ [8], yielding τ_d=~610 ps for SiN_x film having thermal diffusivity, D=1.7×10^{-6} m^2/s.

Hence, at the time of peak heating to 2450°C, the SiN_x has exceeded the sublimation temperature (~1900°C) to initiate the planar microexplosion process against the cold solid SiN_x segments before diffusion would have otherwise had sufficient time (610 ps) to cool and condense the dense vapour phase. As a consequence, the simultaneous heating and microexplosion of periodically stacked plasma disks will cleave the film and form the isolated solid disk segments on the $\lambda/2n_{film}$ fringe spacing. Further, one can anticipate as the multiple plasma disks are exploding, inertial confinement by upper segments will delay and reduce the speed of ejection of deeper segments as well as introduce multiple time-delayed shock fronts that can further affect the hydrodynamics controlling the timing and speed of ejection of individual segments according to their depth. These explosive plasma disks thereby promise a new means for machining or cleaving of subwavelength features inside transparent films.

For the case of 1045-nm wavelength irradiation of the SiN_x film, Figure 1F shows the ejection of first and second segments, again forming concentric rings of decreasing diameter that line up with a Gaussian intensity profile of radius ω_o=4.30 μm and peak incident intensity of I_o=1.15×10^{13} W/cm^2. The ejection of the first segment at a radius of 4.14 μm corresponds closely with this ω_o beam radius. This peak exposure intensity (red cross position in Figure 1F) was applied in the calculations of Figure 1C to yield a peak internal intensity of I_{int}=7.24×10^{12} W/cm^2 and a peak electron plasma density of ~30×critical (i.e., 2.99×10^{22} cm^{-3} at 1045 nm). By considering the threshold incident intensity of I_o=4.24×10^{12} W/cm^2 found in Figure 1B to surpass the critical plasma density, one infers critical density to be generated at a radius of 2.95 μm, marked by the red dashed line in Figure 1F. This radius falls ~29% short of the observed 4.14 μm radius of the first segment in Figure 1F, which is sufficiently good matching considering the ~25% uncertainty of the present beam diameter calculations. Hence, one finds the 1045 nm laser interactions to also trigger the quantise film ejections, driven by the strong plasma absorption when the electron density reaches critical at fringe maxima.

The time evolving laser-plasma calculations for 1045-nm wavelength also support the formation of microexplosions on thin plasma disks. Threshold and 2.7× higher intensity exposures at 1045-nm both generated initial electron plasma widths of 75 nm that narrowed to 17.5 nm at 213 fs (Figure 1H, red dashed line) and to 42.8 nm at 18 fs (Figure 1H, red line), respectively, by nonlinear processes on the optical fringe maxima. Again, these minima correspond to the times at which impact ionisation rates have reached their maxima in Figure 1G for the threshold (red dashed line) and high intensity (red line) exposures at 1045 nm. Thereafter, the electron density widths broaden to 24.8 nm and 138 nm, respectively, by the end of the 340-fs pulse. Through this study of low-to-high intensity exposures, the calculated electron plasma disk widths remain significantly narrower than the 261-nm fringe-to-fringe spacing, supporting the driving of microdisk explosions over a broad range of laser exposures. The results for larger spot sizes are similar to the results with tighter focusing condition of ω_o=0.494 μm at 522-nm wavelength previously presented in reference [8], and this larger size ejection provides a new means for machining or cleaving subwavelength features inside large transparent films.

4.2 Morphology and wavelength scaling of quantised film ejection

A more quantitative evaluation of the quantised film ejections is now followed. A comparison of high and low laser fluence exposure for 515 nm was previously presented in Figure 1D and E, where quantised ejection varied from seven to three segments over an ~18-fold change in average fluence from 76.7 J/cm^2 and 4.4 J/cm^2, respectively. This sequence of deepening quantised ejection with increasing fluence followed the trends as first reported for 522 nm [8]. The SEM image in Figure 1F provides the first evidence of ejection zones appearing on a larger spacing that is commensurate with the longer 1045-nm wavelength. The observation of thicker segments that match with the $\lambda/2n_{film}$=261.3 nm fringe spacing thus validates that quantised film ejection may be controllable with the laser wavelength.

Figure 2 presents higher resolution images of ion-milled samples of SiN_x film with thickness of d=800 nm, where ejection depths are compared over three laser wavelengths of 515 nm, 800 nm and 1045 nm. The oblique top (Figure 2i) and cross-sectional views (Figure 2ii) show quantised ejections by 515 nm (Figure 2Ai,ii), 800 nm (Figure 2Bi,ii) and 1045 nm (Figure 2Ci,ii) wavelength exposures made with average fluences of 2.3 J/cm^2, 0.8 J/cm^2 and 2.0 J/cm^2, respectively. These modest fluences were

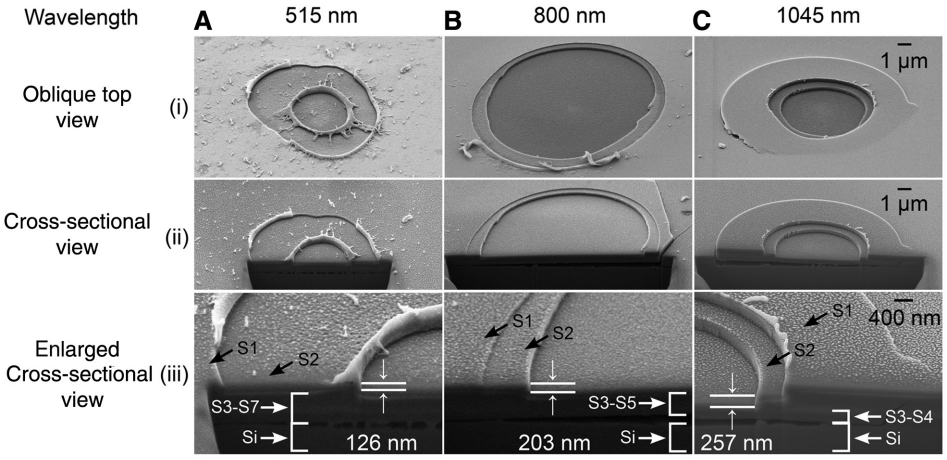

Figure 2 Scanning electron microscopy (SEM) (i) oblique top view, (ii) cross-sectional view and (iii) enlarged cross-sectional view images of 800 nm thick SiN_x film following quantised ejection with incident light at wavelengths of (A) 515 nm, (B) 800 nm and (C) 1045 nm and fluences of 2.3 J/cm², 0.8 J/cm² and 2.0 J/cm², respectively. The full quantised ejection thicknesses of (A,iii) 126 (±5) nm, (B,iii) 203 (±5) nm and (C,iii) 257 (±5) nm were measured at incident wavelengths of 515 nm, 800 nm and 1045 nm, respectively. S1 to S7 represents film separated into seven $\lambda/2n_{film}$ segments.

selected to cleanly remove first and second segments, and thus provide a measure of the full $\lambda/2n_{film}$ fringe spacing in the second segment thickness without inducing significant laser damage to the film. The measured thicknesses of 126 (±5) nm (λ=515 nm), 203 (±5) nm (λ=800 nm) and 257 (±5) nm (λ=1045 nm) from the enlarged cross-sectional images in Figure 2Aiii, Biii, and Ciii, respectively, accurately follow the expected wavelength scaling of fringe spacing of $\lambda/2n_{film}$=128.8 nm, 200 nm and 261.3 nm, respectively, to ±2% experimental uncertainty.

The morphology of the periodic cleavage planes appears to be sharper for longer laser wavelength exposure as shown in the enlarged cross-sectional SEM images in Figure 2iii. The ejection of sharply defined thin segments in the case of 800 nm (Figure 2B) and 1045 nm (Figure 2C) compared with the melted cleavage lips seen for 515 nm (Figure 2A) may be due to the lower laser heating density required to reach a critical plasma density that decreases with wavelength, scaling as $n_{cr} \alpha \lambda^{-2}$. This lower heating may be working together here with the 1.5× thinner plasma disk found for the 1045 nm (red dashed line) versus 515 nm (green dashed line) cases in Figure 1H when at the near threshold exposure, I_{int}. However, the pulse duration also appears to play a significant role as noted by the cleanest segment ejection seen without any melt formation in Figure 2Biii for a short 50-fs exposure at 800-nm wavelength. This ejection is much cleaner than for the 515 nm case (Figure 2A), while one also finds small ~75-nm melt zones intermittently along the rim of the first ejection segment as seen in Figure 2Ciii for the case of longer 340-fs exposure at 1045-nm wavelength. Thermal diffusion during a longer laser interaction time of picoseconds is expected [8] to broaden the laser heating disks, but not during the sub-picosecond pulse durations used in the present study (Table 1). Other forms of thermal or electron transport, as well as shock-front physics, may need to be considered here to understand the underlying role of the short pulse driven laser film ejection.

Strong linear laser interactions in the silicon substrate are usually observed to damage the SiN_x/silicon interface in parallel with the nonlinear plasma excitation that ejects quantised segments from the overlying SiN_x film. In the high exposure case of Figure 1D, the interface has become delaminated, and formed into a nanovoid at the radial position (1.9 μm) of moderately low laser intensity that lines up directly below the threshold zone for ejection of only the first film segment. The interface appears closed at intermediate radii (1.3 μm–0.6 μm), possibly owing to shock recoil from exploding upper segments that push down on the lower segments to possibly fuse and re-bond the SiN_x film to the silicon. Unlike the nonlinear SiN_x film interactions, strong laser heating in the silicon substrate is anticipated to small penetration depths varying from $1/\kappa_{Si}$=25 nm for 515 nm to ~1 μm for 1045 nm, and underlies the laser ejection of the full dielectric layer as reported in references [13, 15, 17–27]. The SiN_x/Si interface damage is also found at lower fluence exposures of 2.3 J/cm², 0.8 J/cm² and 2.0 J/cm² over the various wavelengths of 515 nm (Figure 2Aiii), 800 nm (Figure 2Biii) and 1045 nm (Figure 2Ciii), respectively. The high ~1 μm penetration depth at λ=1045 nm may be responsible for creating a thicker and more stressing heat zone in comparison with

the shorter 515-nm and 800-nm wavelengths, and thus more readily drive ejection of the full film thickness as seen to 7.0-μm radius in Figure 2C. Alternatively, a thin heating zone (~25 nm) may underlie the roughened interface surfaces seen under intermediate fluence values as shown in Figure 2Aiii for λ=515 nm and discussed further in the next section.

4.3 Fluence-control of quantised ejection

A sequence of quantised segment ejections progressing to peel open deeper layers of the SiN_x film were found to be reproducible with increasing laser fluence for all three wavelengths studied. A representative example is given in Figure 3A–H for 800-nm thick SiN_x film irradiated with a pulse energy of 1.67 μJ. The spot sizes varied from ω_o=0.83 μm–16.3 μm, providing average fluences ranging from 76.7 J/cm^2 (Figure 3A) to 0.2 J/cm^2 (Figure 3H), respectively, that drove ejection of all seven segments at the highest fluence or marked a near-threshold exposure for interface damage without blistering or ejection at the lowest fluence. The sequence of oblique top (Figure 3i) and cross-sectional views (Figure 3ii) show a discrete number of ejected segments that reduce sequentially as seven, six, five, three, two, one, one, and zero segments over the respective fluence values reported in each figure (Figure 3i). Each of the cross-sectional SEM images in Figure 3Aii–Gii reveal the depth of first layer ejected segment to be ~95 (±5) nm that matches with the first predicted fringe position of 91.8 nm from the top surface (Figure 1A). All deeper ejected zones, except for the seventh segment, are seen in Figure 3Aii–Eii to form single-segment ejection depths of ~126 (±5) nm that agrees closely with the expected $\lambda/2n_{film}$=128.8 nm fringe spacing, thus confirming that plasma cleavage planes are precisely following on the fringe maxima.

The SEM cross-sectional images in Figure 3ii also reveal delamination of the SiN_x film at the SiN_x/Si interface for all the fluence values shown. At the highest fluence of 76.7 J/cm^2 (Figure 3Aii), this delamination is seen only in an annular zone at larger radii of 1.3 μm–1.9 μm, which surrounds an annular zone over a 0.6-μm–1.3-μm radius where the interface appears to have rebonded. In the central highest intensity zone of <0.6-μm radius, all seven segments have been fully ejected. An explosive interface interaction here is seen to have driven strong pressure or shock waves, ablating and pushing the silicon surface by ~480 nm below the original SiN_x/Si interface. This interface shift decreased to 400 nm and 300 nm at lower laser fluences of 24.2 J/cm^2 (Figure 3Bii) and 8.9 J/cm^2 (Figure 3Cii), respectively, and was not evident at fluences

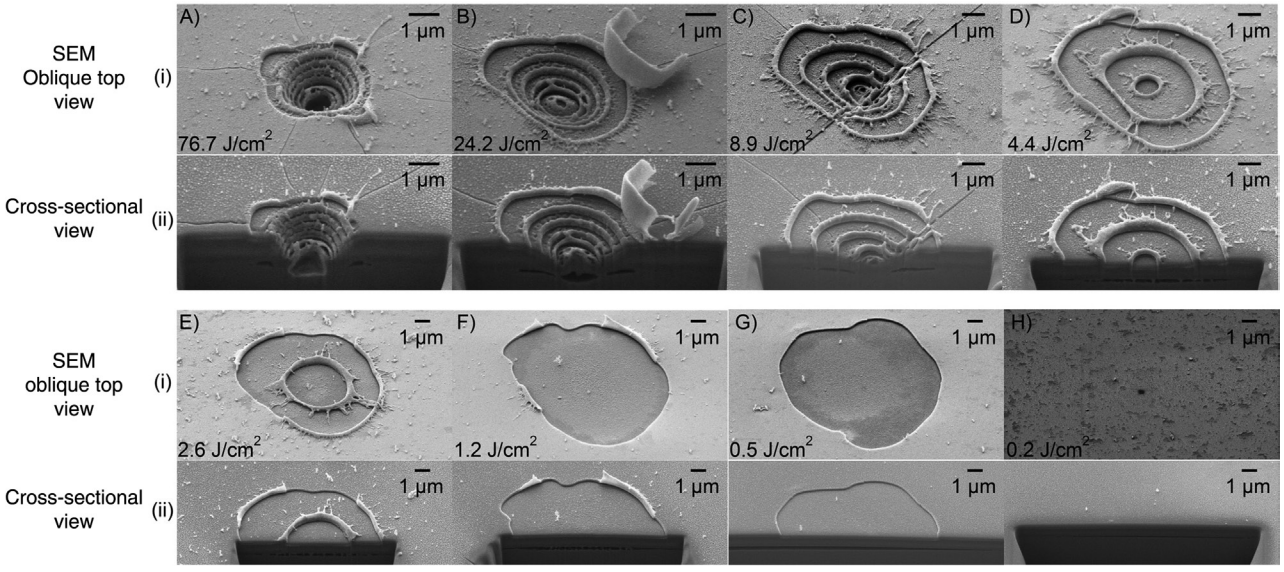

Figure 3 (i) Scanning electron microscopy (SEM) top view and (ii) cross-sectional view images of 800 nm thick SiN_x film following quantised ejection with incident laser light at a wavelength of 515 nm and fluences of (A) 76.7 J/cm^2, (B) 24.2 J/cm^2, (C) 8.9 J/cm^2, (D) 4.4 J/cm^2, (E) 2.6 J/cm^2, (F) 1.2 J/cm^2, (G) 0.5 J/cm^2 and (H) 0.2 J/cm^2, ejecting 7, 6, 5, 3, 2, 1, 1 and 0 segment layer(s), respectively. At high fluences of 76.7 J/cm^2 to 8.9 J/cm^2, (A) to (C) show strong compressive shocks have pushed downward on the central beam area of the SiN_x/Si interface. At moderate fluences of 4.4 J/cm^2 to 1.2 J/cm^2, (D) to (F) show microcavities to have opened at the SiN_x/Si interface in the central beam zone, having structurally roughened surfaces. At low fluences of 0.5 J/cm^2 to 0.2 J/cm^2, (G) and (H) show microcavities have formed at the SiN_x/Si interface with smooth surfaces.

below 4.4 J/cm^2 (Figure 3D–H). One also notes the zone of shock driven fusion of the interface to narrow with decreasing fluence from 0.6-μm–1.3-μm annular radius at 76.7-J/cm^2 fluence (Figure 3Aii) to 0.6-μm–0.9-μm radius at 24.2-J/cm^2 fluence (Figure 3Bii), and then form into a central fused zone of 0.8-μm radius at 8.9-J/cm^2 fluence (Figure 3Cii). The outer annular zone of delamination also follows this shrinking annular fusion zone with the decreasing fluence, where eventually shock-driven fusion is no longer available, leading to a delaminated SiN_x/Si interface over the full laser exposure spot as seen for all the low fluence cases reported in Figure 3D–H. At intermediate fluences of 4.4 J/cm^2 (Figure 3Dii), 2.6 J/cm^2 (Figure 3Eii) and 1.2 J/cm^2 (Figure 3Fii), these delamination zones opened to gaps in the range of 140 nm–180 nm, formed by uneven, corrugated surfaces and occasionally connected by pillars of various shapes. With further reduction of laser fluence to near (0.5 J/cm^2) and below (0.2 J/cm^2) threshold, Figure 3Gii and Hii, respectively, show a large diameter delamination at the SiN_x/Si interface to form smooth interface surfaces separated by a smaller ~40-nm gap. Such smooth interfaces may arise from stress relief at the laser-heated interface, below the threshold for creating large melt zones and driving strong shocks from multiple plasma disk explosions in the overlying SiN_x film.

4.4 Ablation plume bursts

The laser wavelength defines the thickness of segments that may be ejected from a thin film as shown in Figure 2, while the laser fluence provides the opportunity to control the number of ejected segments as shown in Figure 3. One further finds the ejected segments to remain intact, for example, as seen by the near-fully ejected SiN_x segment in Figure 3B. The survival of the thin nanofilm following ablation suggests that laser-formed plasma disks are largely contained, and do not burn through the full thickness of each SiN_x segment over the short pulse duration of the laser. Longer pulse duration would otherwise be expected to melt or vaporise, and destroy the thin film segment.

The sequence of time delayed segment ejections can be anticipated by considering the moment that critical plasma density is first reached at the first and topmost fringe position. Strong plasma reflection and attenuation is expected here to reduce the forward propagating beam intensity and thus diminish the interaction strength at the deeper fringe maxima positions. As the laser fluence is increased to compensate for the plasma shielding, deeper fringe positions may also reach critical plasma density, resulting in ejection of deeper and multiple film segments. However, ejection of deeper segments may be delayed in time due to inertial confinement by the upper segment layers, and particularly by the shock pressure created as upper plasma disks reach threshold first and explode, and push downward against segments delayed in their plasma disk explosions. This combination of multiple plasma disk explosions in the film that take place against a solid silicon substrate therefore favours time-delayed ejections of segments sequentially starting from the top segment, as we first reported in [8].

The sequential ejection of segments was investigated with a side-view ICCD camera system that monitors the light emission of the ablation plume generated by the laser-plasma cleavage of the film into segments. Figure 4A shows the ICCD images of plume emissions recorded at

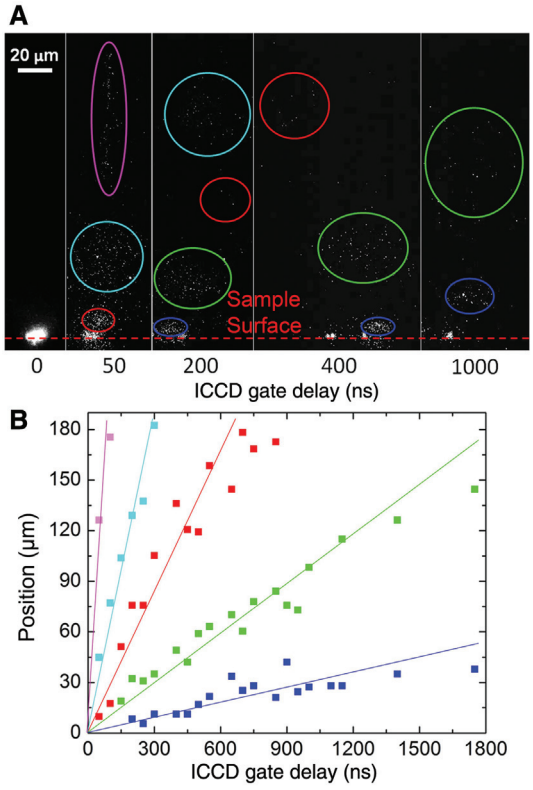

Figure 4 Time-resolved ICCD images (A) of ablation plumes recorded transversely from a 500 nm SiN_x film exposed to 7 J/cm^2 laser fluence. The plume emissions (A) appear in several clusters associated with the ejection of segments 1 (S1) (purple) in the 50 ns–100 ns window, 2 (S2) (cyan) in the 50 ns–300 ns window, 3 (S3) (red) in the 50 ns–850 ns window, 4 (S4) (green) in the 150 ns–1750 ns window and 5 (S5) (blue) in the 200 ns–1750 ns window. The observed positions of clusters of ejected plumes from the film surface are plotted in (B) as a function of the time after laser exposure.

the labelled time delays for a 50-ns gate width, and generated from a 500 nm thick SiN_x film exposed at 522-nm wavelength with a 7-J/cm^2 fluence over a 2.4-µm diameter top-hat beam profile. The images show discrete, isolated plume clusters, as encircled by different coloured rings, to have been ejected with highly different velocities. With higher resolution gating (3 ns), the delayed ejection of the plume clusters becomes clearly evident for the deeper segments, as reported previously [8].

The positions of each cluster group were followed as a function of time up to ~190-µm distance from the film surface and plotted as a function of time in Figure 4B. Five distinct plume segments were clearly identified that agree with the maximum number of segment layers expected to be removed in a 500 nm thick film. SEM images (not shown) confirmed the removal of the five segments at this laser exposure condition. A linear representation of the plume positions (coloured lines in Figure 4B) with the ICCD camera gate delay revealed a high ejection speed of 1.7 km/s that was associated with the first segment, and falling ~50-fold to 0.03 km/s for the bottom (fifth) segment. This unusual 'bursting' of laser ablation plume is not seen in typical laser ablation processes, where material is removed continuously from the top surface to form a single cluster of plume emission following each laser pulse. Hence, the bursting of isolated plume clusters in Figure 4A attests to discrete quantised segments, ejected by the laser-plasma cleavage at the laser fringe maxima. Moreover, the inertial confinement that upper exploding plasma disks impose against lower exploding segments favours a concentration of the dissipated laser energy into the topmost ejected disk that is believed to underpin this ~50-fold higher ejection speed of this first segment against the deepest segment for the present film and laser exposure condition in Figure 4.

Similar plume bursts were previously reported [8] for the same film thickness and exposure wavelength (522 nm), however, with a Gaussian beam profile. For 2× higher exposure fluence of 13.7 J/cm^2, five cluster groups were followed with a higher gating resolution (3 ns and 10 ns), revealing two to three times faster ejection speeds [8] (Figure 3C) than in Figure 4. However, the Gaussian beam case revealed a clustering of the plume segments that were associated with fusion of the first and second segments as well as the third and fourth segments as seen in SEM cross-sectional images [8], (Figure 3B). Such fusion and ejection speed effects are evidence of strong shock front physics as multiple plasma disks are exploding in the thin film. With lower fluence exposure, the ICCD imaging could closely follow a diminishing number of plume clusters that are commensurate with the reduced number of ablated segments, as observed by SEM imaging, for example, in Figure 3. The lower fluence exposure also reduced the ejection speed of the cluster groups as expected by the lower density plasma generation seen with the simulation (i.e., Figure 1B with respect to 1C).

Time-resolved *in situ* ICCD imaging of plume bursts has confirmed the thin-film laser interference effects on forming laser-plasma cleavage planes, enabling the quantised structuring of SiN_x thin films. Furthermore, ICCD imaging provided a richer evidence of the sequential nano-plasma disk explosions, and their competition in terms of shock front physics that enhances or delays the ejection of segments according to their depth. One also finds that adjacent segments will fuse reproducibly under certain exposure conditions that otherwise were above the threshold exposure for cleaving. Further plume studies of nanodisk ejections that can follow the shock dynamics of multilayered plasma planes are promising to open additional pathways for controlled cleavage and nanostructuring of thin transparent films.

5 Applications of quantised ejection

Numerous application directions have been previously identified [8] that may emerge from various combinations of quantised surface ejection and nanovoid formation in thin films, including nanocleaving, marking, colouring, multilevel structuring, free-standing nanofilm, nanofluidics, microlenses and lab-in-film devices. Previously, large area structuring was demonstrated by stitching together arrays of small (~1.5-µm diameter) individual exposure spots, but leading to poorly connected structures with poor surface morphology [8]. In this section, we take advantage of higher laser pulse energy to extend the radial reach of laser interaction first reported in Kumar et al. [8], and present larger area examples of free-standing blisters and nanovoids, and particularly examine the prospects for film colouring.

5.1 Thin-film interference colouring

The thin-film interference effect defines the colours observed from films, which we seek to manipulate by quantised thinning and nanovoid generation of the SiN_x film. The formation of a nanovoid in the film or the delamination of the SiN_x film at the SiN_x/Si interface both introduce a π phase correction on the Fresnel reflection

coefficient with respect to the π-shift expected from the usual SiN_x-to-Si interface reflection. The quantised film thinning and phase shifting effects are investigated here for film thicknesses of 500-nm (Figure 5A–C) and 800-nm (Figure 5D and E) and with 515-nm laser exposure for Gaussian beam profiles to create >6-µm diameter coloured spots, as shown in Figure 5.

The primary interference effects are followed as forming only between the first two interfaces seen by the top illuminating laser light, and therefore fall into either air-SiN_x-Si or air-SiN_x-air interface cases. Given a film thickness of d, the resonant wavelengths, λ_k, for high reflection at normal incidence can be found in Eq. (6):

$$\lambda_k = \frac{2dn_{\text{film}}}{k} \tag{6}$$

for the air-SiN_x-Si case, or in Eq. (7):

$$\lambda_k = \frac{2dn_{\text{film}}}{k - \frac{1}{2}} \tag{7}$$

for the air-SiN_x-air case. In both equations, k is an integer value of the order of interference.

Figure 5i shows the optical images of laser-coloured spots and with the corresponding SEM images (Figure 5ii–iv) formed over average fluence exposure of 0.23 J/cm² (Figure 5A), 0.45 J/cm² (Figure 5B) and 1.20 J/cm² (Figure 5C) for 500-nm thick SiN_x film, and 0.5 J/cm² (Figure 5D) and 1.2 J/cm² (Figure 5E) for 800-nm thick SiN_x film. For the case of unprocessed SiN_x-film on an Si substrate, Eq. (6) anticipates strong reflections at several resonance wavelengths in the visible spectrum, namely ~667 nm (red), ~500 nm (green) and ~400 nm (violet) for d=500 nm, and ~640 nm (red), ~533 nm (green), ~457 nm (blue) and ~400 nm (violet) for d=800 nm. However, compensating for the human eye sensitivity peaking at ~550-nm wavelength, one finds only the dominating resonant wavelengths to match with the observed green and muddy green colours seen outside the laser processing zones for the 500-nm (Figure 5Ai, Bi and Ci) and 800-nm (Figure 5Di and Ei) thick films, respectively.

Eq. (6) may also be applied to assess the dark red colour observed in the central cavity of Figure 5Ci. Here, a moderately high fluence of 1.20 J/cm² ejected three segments, thinning the film to d=174 (±5) nm thickness as seen in the SEM cross-section image (Figure 5Civ). Following the vertical red dashed lines in Figure 5Ci, through the SEM top (Figure 5Cii) and cross-sectional views (Figure 5Ciii and Civ), one anticipates a shock wave front to have fused together the remaining fourth and fifth segments, and further driven this segment pair to fuse back to the Si substrate without delaminating. Eq. (6) only provides for a single reflection peak of 696 nm in the visible spectrum, matching with the observed dark red colour as shown in Figure 5Ci.

The light blue colour seen in the central 5.5-µm radial zone of Figure 5Ai and in an annular zone of 3.7-µm–5.3-µm radius in Figure 5Bi represent zones of approximately

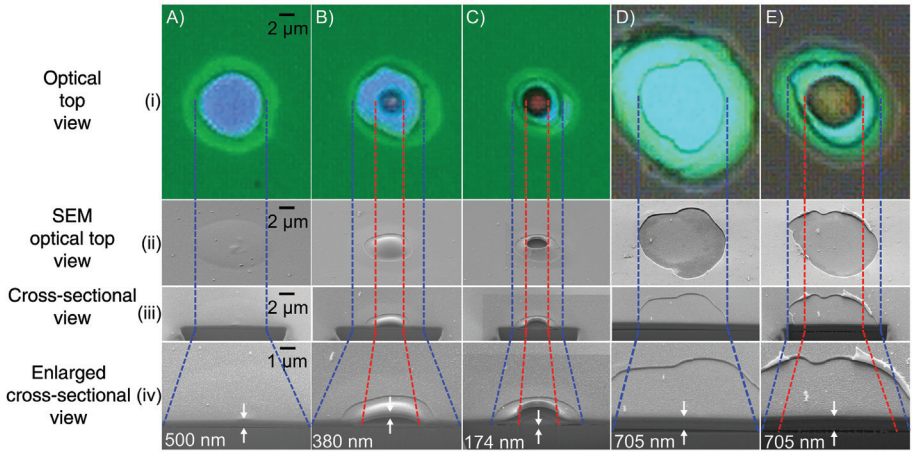

Figure 5 (i) Optical top view, (ii) scanning electron microscopy (SEM) oblique top view, (iii) cross-sectional view and (iv) enlarged cross-sectional view images of (A–C) 500 nm thick and (D, E) 800 nm thick SiN_x films exposed to 515 nm wavelength light of Gaussian beam profile and fluences of (A) 0.23 J/cm², (B) 0.45 J/cm², (C) 1.20 J/cm², (D) 0.5 J/cm² and (E) 1.2 J/cm². The SiN_x thickness of the blisters formed against nanovoids (inside the red dash lines) has been reduced to (Biii) 380 (±5) nm and (Ciii) 174 (±5) nm and generated film colours of (Bi) violet and (Ci) dark red, respectively. Larger areas, as seen inside the blue dashed lines, have formed between the SiN_x film and air to produce strong (Ai and Bi) blue, (Ci) greenish blue and (Di and Ei) green reflections. The dull brown colour as seen inside the red dashed line in (Di) is due to the roughened SiN_x interface after delamination.

equal fluence exposure of 0.23 J/cm^2. Following the blue dashed lines through the respective SEM micrographs, one finds the SiN_x/Si interface has delaminated, requiring the application of Eq. (7) to calculate the resonant wavelength reflections. Accounting for no segment ejection in both of these zones (i.e., d=500 nm), two visible reflection resonances were calculated at ~571 nm (yellow) and ~444 nm, combining to match with the observed light blue colour. At the higher fluence exposure in the central zone (radius <1.9 μm) in Figure 5B, the red dashed line encloses a processing zone of SiN_x film thinned to d=380 (±5) nm by ejection of one segment and nanovoid formation by plasma disk explosion at the fourth fringe position, together with fusion of the second, third and fourth film segments. This blister defines a free-standing film of 1.9-μm radius, which is 4.6 times larger than the blisters previously presented in reference [8]. Application of Eq. (7) yields visible spectral reflection peaks at ~608 nm (orange) and ~434 nm (violet) that combine to match with the observed violet colour.

Several examples are present of ejection of the first segment together with delamination at the SiN_x/Si interface as seen in Figure 5C (between red and blue dashed lines), D (following the blue dashed line) and E (following the blue dashed line) that were formed with moderate fluence of ~0.5 J/cm^2–1.2 J/cm^2. Application of Eq. (7) for the 450 (±5) nm film thickness yields eye-visible reflection resonances at ~514 nm (green) and ~400 nm (deep violet), matching with the observed greenish blue colour as seen between the red and blue dashed lines in Figure 5C. Following the blue dashed lines in Figure 5D and E, the observed film thickness of 705 (±5) nm for a delaminated SiN_x/Si interface predicts via Eq. (7) the strong visible reflection resonances at ~627 nm (orange red), ~513 nm (green) and ~434 nm (violet). However, the green colour is dominating here, because of the strong human eye sensitivity peaking at ~550-nm wavelength.

An examination of the delaminated SiN_x/Si interface surfaces in the central exposure zones under a low fluence of 0.5 J/cm^2 (Figure 5D) and a moderate fluence of 1.2 J/cm^2 (Figure 5E) reveals the contrasting smooth (Figure 5Div) and rough (Figure 5Eiv) surfaces, respectively. The smooth interface of Figure 5Div provides a highly clean, non-scattering interface for the resonant green light reflection from the zone demarked by the blue dashed line (Figure 5Di), whereas the roughened interface of Figure 5Eiv contained by the red dashed line is found to optically scatter light as seen by the dull brown colour in Figure 5Ei. Hence, the formation of smooth-surfaced in-film nanovoids and delaminated SiN_x/Si interfaces are most desired, which in combination with the quantised thinning of SiN_x film by the controlled incident laser intensity, are attractive to provide a broader spectral colour control and patterning in thin dielectric film. Moreover, this laser-film colouring can be further broadened to any desired colour by varying the initial film thickness, the laser wavelength, or the laser incident angle, as well as by changing the viewing angle from the present case of normal incidence. The present laser-film cleaving method therefore extends beyond current laser-colouring techniques such as laser-induced periodic surface structures (LIPSS) [28] and laser surface oxidation [29]. However, the laser interference cleaving promises more precise control than seen in surface rippling and without the need for driving material compositional changes.

6 Summary

In this paper, we demonstrated a novel technique for sub-wavelength axial structuring of thin dielectric film on a high refractive index substrate, by harnessing the nonlinear laser-material interaction of femtosecond laser light together with thin film interference effects. A quantised array of narrow plasma disks are inferred to have formed inside the film following on the $\lambda/2n_{film}$ interferometric periodic spacing. Such effects are anticipated for thin film thickness $>\lambda/4n_{film}$, and where Fresnel reflections from the air/film and film/substrate interfaces are sufficiently strong to create a substantially contrasting Fabry-Perot intensity modulation. Modelling of the strong nonlinear laser interactions predicted the generation of narrow plasma zones of 17.5 nm–42.8 nm thickness that reach the threshold for laser cleaving when intensities reach the threshold for driving plasma density to critical density. The wavelength dependence of quantised ejection precisely followed the $\lambda/2n_{film}$ fringe spacing over 515-nm–1045-nm wavelength lasers as validated in Figure 2. Further, the number of segment ejections was shown to be precisely controlled by the laser fluence in Figure 3. The predicted plasma disks were shown by ICCD imaging in Figure 4 to validate the quantised ejection of multiple segments, creating a burst of ejected plume in a temporal sequence. This new form of high-resolution film patterning opens new directions in 3D surface nanopatterning, marking and colouring by precisely controlling the formation of internal cavities and digital removal of thin film with a precision of $\lambda/2n_{film}$. In addition to cosmetic and surface patterning applications, internal cavities can be further generated to fabricate free-standing thin film that is attractive in microelectronic, photonic and micro electro-mechanical systems (MEMS) applications, as well as opening the possibility for lab-in-film devices.

7 Contributions

P.R.H. conceived this study and oversaw all aspects of the research study, which was aimed to extend on the preliminary experimental and modelling work by K.K., K.K.C.L. and J.L. as reported in Kumar et al. [8]. Films were grown by K.K. and S.H. S.H. designed and carried out the film ejection experiments on various laser systems partly supported by J.L., and completed the morphological analysis. J.L. completed the ICCD plume study and data analysis and contributed to the writing of Section 4.4. K.K.C.L. developed the thin film models and carried out the simulations with significant additional contributions by K.K. and S.H. The film colour assessment was made by S.H. K.K. prepared the introduction and background sections. S.H. wrote all of the remaining manuscript sections. S.H. and P.R.H. organised the manuscript layout, integrated all contributions and completed the final form of the paper.

Acknowledgments: We thank the Canadian Centre for Electron Microscopy at McMaster University, which is supported by the Natural Sciences and Engineering Research Council of Canada (NSERC) and other government agencies, for performing the SEM and focused ion beam work. This work was supported by NSERC and the University of Toronto.

References

[1] M. Campbell, A. J. Turberfield, D. N. Sharp, M. T. Harrison and R. G. Denning, Nature 404, 53–56 (2000).
[2] K. O. Hill, Y. Fujii, D. C. Johnson and B. S. Kawasaki, Appl. Phys. Lett. 32, 647–649 (1978).
[3] M. Mero, B. Clapp, J. C. Jasapara, W. Rudolph, D. Ristau, et al., Opt. Eng. 44, 51107-1–51107-7 (2005).
[4] M. Mero, A. J. Sabbah, J. Zeller and W. Rudolph, Appl. Phys. A 81, 317–324 (2005).
[5] J. Jasapara, A. V. V. Nampoothiri, W. Rudolph, D. Ristau and K. Starke, Phys. Rev. B 63, 045117-1–045117-5 (2001).
[6] Y. Hosokawa, M. Yashiro, T. Asahi and H. Masuhara, J. Photochem. Photobiol. A 142, 197–207 (2001).
[7] Y. Hosokawa, M. Yashiro, T. Asahi, H. Masuhara, T. Kadota, et al., Jpn. J. Appl. Phys. 40, L1116–L1118 (2001).
[8] K. Kumar, K. K. C. Lee, J. Li, J. Nogami, N. P. Kherani, et al., Light Sci. Appl. 3, e157 (2014).
[9] L. Schermelleh, S. Thalhammer, W. Heckl, H. Pösl, T. Cremer, et al., BioTechniques 27, 362–367 (1999).
[10] K. Miura, J. Qiu, H. Inouye, T. Mitsuyu and K. Hirao, Appl. Phys. Lett. 71, 3329–3331 (1997).
[11] R. R. Gattass and E. Mazur, Nat. Photon. 2, 219–225 (2008).
[12] E. N. Glezer and E. Mazur, Appl. Phys. Lett. 71, 882–884 (1997).
[13] J. P. McDonald, M. D. Thouless and S. M. Yalisove, J. Mater. Res. 25, 1087–1095 (2010).
[14] J. P. McDonald, V. R. Mistry, K. E. Ray and S. M. Yalisove, Appl. Phys. Lett. 88, 183113-1–183113-3 (2006).
[15] J. P. McDonald, V. R. Mistry, K. E. Ray, S. M. Yalisove, J. A. Nees, et al., Appl. Phys. Lett. 88, 153121-1–153121-3 (2006).
[16] T. Rublack and G. Seifert, Opt. Mater. Express 1, 543–550 (2011).
[17] T. Rublack, S. Hartnauer, P. Kappe, C. Swiatkowski and G. Seifert, Appl. Phys. A 103, 43–50 (2011).
[18] T. Rublack, M. Schade, M. Muchow, H. S. Leipner and G. Seifert, J. Appl. Phys. 112, 023521-1–023521-7 (2012).
[19] K. Kumar, K. K. C. Lee, P. R. Herman, J. Nogami and N. P. Kherani, Appl. Phys. Lett. 101, 222106-1–222106-5 (2012).
[20] J. Bohandy, B. F. Kim and F. J. Adrian, J. Appl. Phys. 60, 1538–1539 (1986).
[21] G. Westphal, R. Burgemeister, G. Friedemann, A. Wellmann,N. Wernert, et al., Method. Enzymol. 356, 80–99 (2002).
[22] E. G. Gamaly, A. V. Rode, B. Luther-Davies and V. T. Tikhonchuk, Phys. Plasmas 9, 949–957 (2002).
[23] X. Jing, Y. Tian, J. Zhang, S. Chen, Y. Jin, et al., Appl. Surf. Sci. 258, 4741–4749 (2012).
[24] K. X. Wang, Z. Yu, V. Liu, Y. Cui and S. Fan, Nano Lett. 12, 1616–1619 (2012).
[25] Q. Sun, H. Jiang, Y. Liu, Z. Wu, H. Yang and Q. Gong, Opt. Lett. 30, 320–322 (2005).
[26] B. R. Tull, J. E. Carey, E. Mazur, J. P. McDonald and S. M. Yalisove, MRS Bull. 31, 626–633 (2006).
[27] J. P. McDonald, A. A. McClelland, Y. N. Picard and S. M. Yalisove, Appl. Phys. Lett. 86, 264103-1–264103-3 (2005).
[28] A. Y. Vorobyev and C. Guo, Appl. Phys. Lett. 92, 041914-1–041914-3 (2008).
[29] A. Pérez del Pino, P. Serra and J. L. Morenza, Thin Solid Films 415, 201–205 (2002).

Stephen Ho
Edward S. Rogers Sr. Department of Electrical and Computer Engineering, University of Toronto, 10 King's College Road, Toronto, Ontario M5S 3G4, Canada,
stephen.ho@utoronto.ca

Stephen Ho is a postdoctoral fellow at the University of Toronto. His interest in Biomedical Engineering led him to study Engineering Science at the University of Toronto and received his B.A.Sc. degree in 2002. He furthered his studies and he received his M.A.Sc. degree (2005) and PhD (2013) in Electrical and Computer Engineering under the Photonics Group at the University of Toronto. The title of Stephen's thesis was 'Femtosecond Laser Microfabrication of Optofluidic Lab-on-a-Chip with Selective Chemical Etching'. Stephen now continues his research interest and works on femtosecond laser micro and nano-machining, laser fabrication of optofluidic lab-on-a-chip and 3-D structures inside transparent dielectric materials.

Kitty Kumar
Wyss Institute for Biologically Inspired Engineering, Harvard University, Boston, MA, USA

Kitty Kumar is a postdoctoral fellow at Harvard University. She earned her first MSc in the Department of Physics at Panjab University, India. Her fascination with manipulating materials at nano-scale to change their properties for a broad range of applications by using fundamental science and advance tools led her earn second MSc degree in Physics at Memorial University, Canada followed by PhD in Materials Science and Engineering at the University of Toronto. She is focused on developing new techniques for engineering materials for various applications and understanding the underlying physical phenomenon. The title of her PhD thesis is “High performance inverted pyramidal texture for silicon photovoltaics”. She now continues her research at Harvard University on bioinspired materials.

Kenneth K.C. Lee
Edward S. Rogers Sr. Department of Electrical and Computer Engineering, University of Toronto, 10 King’s College Road, Toronto, Ontario M5S 3G4, Canada

Kenneth K.C. Lee received his B.A.Sc. degree in Engineering Science from the University of Toronto in 2009. He is currently a PhD candidate in the Department of Electrical and Computer Engineering at the University of Toronto, Ontario, Canada. He is exploring ways to improve polymer-based micro-actuator and to fabricate compact fibre-optic sensors with femtosecond laser direct writing. The miniature and flexible polymer actuator and optical sensor will serve as building blocks to create an advanced steerable biomedical catheter for minimally invasive surgical procedures.

Jianzhao Li
Edward S. Rogers Sr. Department of Electrical and Computer Engineering, University of Toronto, 10 King’s College Road, Toronto, Ontario M5S 3G4, Canada

Jianzhao Li received his BSc degree from Sichuan University, Chengdu, China, his MSc degree from Fudan University, Shanghai, China, and his PhD degree from the University of Electro-Communications, Tokyo, Japan. His research experience has covered laser, laser spectroscopy, nonlinear and quantum optics, laser material processing and micro/nano-fabrication. Currently he focuses on the mechanism study and application development of advanced laser micro/nano-fabrication assisted with 5-dimensional multimodal laser microscopy and spectroscopy. He is a member of OSA and SPIE.

Peter R. Herman
Edward S. Rogers Sr. Department of Electrical and Computer Engineering, University of Toronto, 10 King’s College Road, Toronto, Ontario M5S 3G4, Canada

Peter R. Herman received the B.Eng. degree (1980) in Engineering Physics at McMaster University. He earned M.A.Sc. (1982) and PhD (1986) degrees studying lasers and diatomic spectroscopy in the Physics Department at the University of Toronto followed with a post-doctoral position at the Institute of Laser Engineering in Osaka University, Japan (1987) to the study of laser-plasma physics and X-ray lasers. He joined the Department of Electrical and Computer Engineering at the University of Toronto in 1988 where he currently holds a full professor position. Professor Herman directs a large and collaborative research group that develops and applies laser technology and advanced beam delivery systems to control and harvest laser interactions in new frontiers of 3-D nanofabrication. This includes processing of optical materials aimed at lightwave circuits, microfluidics, optofluidic systems, biophotonic sensors, and smart medical catheters with end goals of new manufacturing processes towards the concepts of lab-on-a-fiber and lab-in-a-film microsystems. Our group has published more than 300 scientific journal and conference papers and generated 10 patents.